Supermassive Black Hole Property Determination via Gravitational Radiation from Eccentrically Orbiting Stellar Mass Black Hole Binaries: Interim Report 2

Andrew Laeuger

July 2022

1 Progress through six weeks

In this work, I am studying prospects for parameter estimation of BBH+SMBH triple systems using space-based GW observatories. In particular, I am extending the work of [4] to the case where the stellar-mass BBH has an eccentric orbit about the central SMBH and investigating how the eccentricity impacts the ability of GW observatories to measure certain relevant parameters.

1.1 Mathematical Description of the SMBH+BBH Triple System

1.1.1 Geometry

$\boldsymbol{\theta^a}$	**Definition**
$\log \mathcal{M}_z$	Detector Frame Chirp Mass: $\mu^{3/5}(m_1+m_2)^{2/5}$
q	Mass Ratio m_2/m_1
$\log D_L$	Luminosity Distance
t_c	Coalescence Time
ϕ_c	Coalescence Phase
$\bar{\theta}_S$,$\bar{\phi}_S$	Line of Sight of BBH+SMBH Triple
$\bar{\theta}_J$,$\bar{\phi}_J$	Orientation of Total Angular Momentum $\boldsymbol{J}$
λ_L	Angle Between $\boldsymbol{L}_i$ and $\boldsymbol{L}_o$
α_0	Initial Phase of $\boldsymbol{L}_i$ Around $\boldsymbol{L}_o$
$\log M_3$	SMBH Mass
$\log a_o$	Outer Orbit Semimajor Axis
γ_o	Outer Orbit Argument of Periapsis
e_o	Outer Orbit Eccentricity
T_o	Time when BBH Reaches Periapsis

Table 1: Relevant parameters in BBH+SMBH triple system for GW observed by detectors. Bars over angles indicate the Solar System coordinate frame.

We first describe the full geometry of the SMBH+BBH triple system and waveform with an eccentric outer orbit. In Figure 1, the barred coordinates demarcate a Solar System centered coordinate system, while the unbarred coordinates demarcate a coordinate system based on the orientation of the space-based GW observatory. In order to compute the antenna response, we need to be able to convert from the unbarred

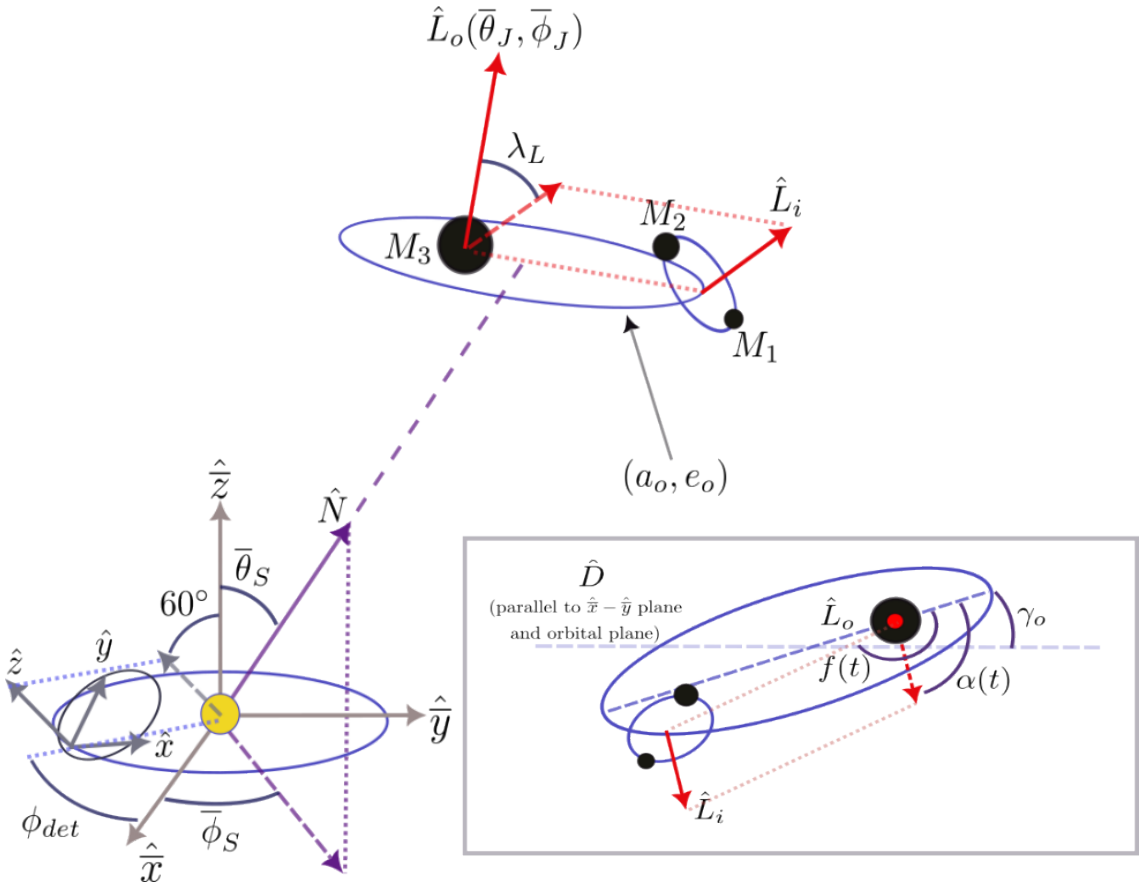

Figure 1: Left: Geometry of the SMBH+BBH triple system. Right, inset: View of the triple system normal to the plane of the outer orbit. See the discussion below and Table 1 for definition of all parameters. Figure dimensions do not give any indication of true scale. In this work, we neglect the precession of γ_o as the BBH orbits the SMBH.

coordinates to the barred coordinates, which is as follows:

$$\hat{x} = -\frac{1}{4}\sin(2\phi_d)\hat{\overline{x}} + \frac{3+\cos(2\phi_d)}{4}\hat{\overline{y}} + \frac{\sqrt{3}}{2}\sin(\phi_d)\hat{\overline{z}} \tag{1}$$

$$\hat{y} = \frac{-3+\cos(2\phi_d)}{4}\hat{\overline{x}} + \frac{1}{4}\sin(2\phi_d)\hat{\overline{y}} - \frac{\sqrt{3}}{2}\cos(\phi_d)\hat{\overline{z}} \tag{2}$$

$$\hat{z} = -\frac{\sqrt{3}}{2}\cos(\phi_d)\hat{\overline{x}} - \frac{\sqrt{3}}{2}\sin(\phi_d)\hat{\overline{y}} + \frac{1}{2}\hat{\overline{z}} \tag{3}$$

The sky location of the hierarchical triple is $(\overline{\theta}_S, \overline{\phi}_S)$, which points along the vector $\hat{N}$, and has a luminosity distance of d_L. The triple itself consists of a BBH with black holes of masses M_1 and M_2, or equivalently, a chirp mass of $\mathcal{M} = \frac{(M_1 M_2)^{3/5}}{(M_1+M_2)^{1/5}}$ and mass ratio of $q = M_2/M_1$, and an SMBH of mass M_3. The shape of the BBH's orbit around the SMBH can be determined entirely (at least to a sufficiently close approximation) by the semimajor axis a_o and the eccentricity e_o.

The unit vector of the angular momentum of the two lighter black holes in the binary system is $\hat{L}_i$, and the unit vector of the angular momentum of the binary's orbit about the SMBH is $\hat{L}_o$. The angle between $\hat{L}_i$ and $\hat{L}_o$ is λ_L. λ_L stays constant in time, but the phase of $\hat{L}_i$, $\alpha(t)$, changes as the coupling between the "spin" of the BBH and the orbit of the BBH about the SMBH induces precession. Using Eq. 9.200 of [2], we find the de Sitter precession frequency

$$\Omega_{dS}(t) = \frac{3}{2}\Omega_o \frac{GM_3}{c^2 a_o(1-e_o^2)}\left[\frac{\left(1+e_o\cos(f(t))\right)^3}{(1-e_o^2)^{3/2}}\right] \tag{4}$$

where $f(t)$ is the true orbital anomaly as shown in the inset of Figure 1. The secular precession rate agrees with that in the introduction of [4]: that is, when integrated over one full orbital period of the BBH around the SMBH, the orbit-averaged de Sitter precession frequency that matches Eq. 1 of [4]. Since

$$\frac{d\hat{L}_i}{dt} = \Omega_{dS}\hat{L}_o \times \hat{L}_i \tag{5}$$

the inner orbit angular momentum $\hat{L}_i$ traces a cone around the outer orbit angular momentum $\hat{L}_o$. The phase of $\hat{L}_i$ in this cone, as shown in the inset of Figure 1, can be found by integrating the time-dependent de Sitter precession rate:

$$\alpha(t) = \alpha_0 + \int_t^{t_c} \Omega_{dS}(t')dt' \tag{6}$$

where α_0 is the phase at the time of the binary coalescence t_c.

Finally, to quantify the Doppler shift, we need to find a few additional parameters. First, the inclination of the outer orbit angular momentum follows

$$\cos\iota_J = \hat{N} \cdot \hat{L}_o \tag{7}$$

Next, the argument of periapsis, γ_o, is defined as the angle between the major axis of the elliptical orbit and the line in space which is parallel to both the plane of the orbit *and* the $\hat{\bar{x}} - \hat{\bar{y}}$ plane. It is well known that an elliptical orbit does not admit an analytical solution for the position in the orbit as a function of time. However, there are some well-established numerical methods for solving this problem. The distance of the BBH from the SMBH is given by

$$r(t) = \frac{a_o(1-e_o^2)}{1 + e_o\cos(f(t))} \tag{8}$$

with $f(t)$ once again being the true orbital anomaly. To find the true orbital anomaly, we must first find the eccentric anomaly, which is similar to the true orbital anomaly except that the origin used for this quantity is the center of the ellipse rather than the focus where the SMBH is located. Kepler's equation gives the relation between the eccentric anomaly u and time:

$$u(t) - e_o\sin(u(t)) = \sqrt{\frac{GM_3}{a_o^3}}(t-T) = 2\pi\frac{t-T}{P_o} \tag{9}$$

where T_o is a constant which denotes the time when the BBH reaches periapsis. We can subtract multiples of $P_o = \frac{2\pi}{\sqrt{GM_3/a_o^3}}$ from $t - T_o$ until it falls between 0 and 1, and then apply Newton's method to find $u(t)$, as this equation does not have an analytical solution. Explicitly, we conduct an iterative process, where $u_1 = 2\pi\frac{t-T_o}{P_o}$ and

$$u_{n+1} = u_n + \frac{u_1 - (u_n - e_o\sin u_n)}{1 - e_o\cos u_n} \tag{10}$$

Usually, only roughly five iterations are needed to obtain high accuracy in $u(t)$. The eccentric anomaly can be converted to the orbital anomaly using

$$\tan\left(\frac{1}{2}f(t)\right) = \sqrt{\frac{1+e_o}{1-e_o}}\tan\left(\frac{1}{2}u(t)\right) \tag{11}$$

1.1.2 Waveform

We can now proceed to calculate the strain detected by the space-based observatory, using the results of [1]. The overall measured signal is

$$\boxed{h_{meas} = h_C\sqrt{(A_+F_+)^2 + (A_\times F_\times)^2}\exp\{-i[\Phi_P + 2\Phi_T + \Phi_D]\}} \tag{12}$$

where h_C is the carrier waveform, A and F are the polarization-dependent amplitude modulation and antenna response, respectively, and Φ_P, Φ_D, and Φ_T are the polarization, Thomas, and Doppler phases. It is this

signal that we use to calculate elements of the Fisher information matrix. Post-Newtonian expansion gives a carrier waveform, in the frequency domain (and geometrized units $G = c = 1$), of

$$\tilde{h}_C(f_{GW}) = \Big(\frac{5}{96}\Big)^{1/2} \frac{\mathcal{M}^{5/6}}{\pi^{2/3} d_L} f_{GW}^{-7/6} \exp\{i[2\pi f_{GW} t_c - \phi_c - \frac{\pi}{4} + \frac{3}{4}(8\pi\mathcal{M} f_{GW})^{-5/3}]\} \tag{13}$$

where ϕ_c is the phase at coalescence. There is an analytical form for the time corresponding to a given GW frequency:

$$t(f_{GW}) = t_c - \frac{5}{256\pi^{8/3}} \frac{1}{\mathcal{M}^{5/3} f_{GW}^{8/3}} \tag{14}$$

The two polarizations of the strain, h_+ and $h_\times$, are modified by the amplitude factors

$$A_+ = 1 + (\hat{L}_i \cdot \hat{N})^2 \tag{15}$$

$$A_\times = -2\hat{L}_i \cdot \hat{N} \tag{16}$$

and furthermore, the detector response F to incoming waves of each polarization varies, as

$$F_+(\theta_S, \phi_S, \psi_S) = \frac{1}{2}(1 + \cos^2\theta_S)\cos 2\phi_S \cos 2\psi_S - \cos\theta_S \sin 2\phi_S \sin 2\psi_S \tag{17}$$

$$F_\times(\theta_S, \phi_S, \psi_S) = \frac{1}{2}(1 + \cos^2\theta_S)\cos 2\phi_S \sin 2\psi_S + \cos\theta_S \sin 2\phi_S \cos 2\psi_S \tag{18}$$

where

$$\tan\psi_S = \frac{\hat{L}_i \cdot \hat{z} - (\hat{L}_i \cdot \hat{N})(\hat{z} \cdot \hat{N})}{\hat{N} \cdot (\hat{L}_i \times \hat{z})} \tag{19}$$

(note the use of the detector-frame coordinates here). The first of the three additional phases is the polarization phase, which allows us to rewrite the signal strain in terms of a single amplitude and a modifying phase, seen in Eq. 12 (as opposed to $h(t) = h_+(t)F_+(t) + h_\times(t)F_\times(t)$). It is given by

$$\tan\Phi_P(t) = -\frac{A_\times(t)F_\times(t)}{A_+(t)F_+(t)} \tag{20}$$

The second is the Thomas phase, which can be understood as the change in signal phase which results from ensuring that the orbital separation vector remains orthogonal to the angular momentum as the angular momentum precesses. It is given by

$$\Phi_T(t) = -\int_t^{t_c} dt \Big[\frac{\hat{L}_i \cdot \hat{N}}{1 - (\hat{L}_i \cdot \hat{N})^2}\Big](\hat{L}_i \times \hat{N}) \cdot \frac{d\hat{L}_i}{dt} \tag{21}$$

The final phase term is the Doppler phase shift, the phase shift induced by the evolving distance between the detector and the GW source. There are two contributions to this phase. The first is the contribution from the detector, given at a particular time t by

$$\Phi_{D,det}(f_{GW}) = 2\pi f_{GW}(1\text{ AU})\sin\theta_S \cos(\phi_{det} - \phi_S) \tag{22}$$

The other is from the source, which is modulated by the changing orbital radius as well as the inclination of the outer orbit and the position of the BBH in that orbit:

$$\Phi_{D,src}(f_{GW}) = 2\pi f_{GW} \frac{a_o(1 - e_o^2)\sin\iota_J}{1 + e_o\cos(f(t))} \sin(f(t) + \gamma_o) \tag{23}$$

noting the difference between the GW frequency f_{GW} and the true orbital anomaly $f(t)$.

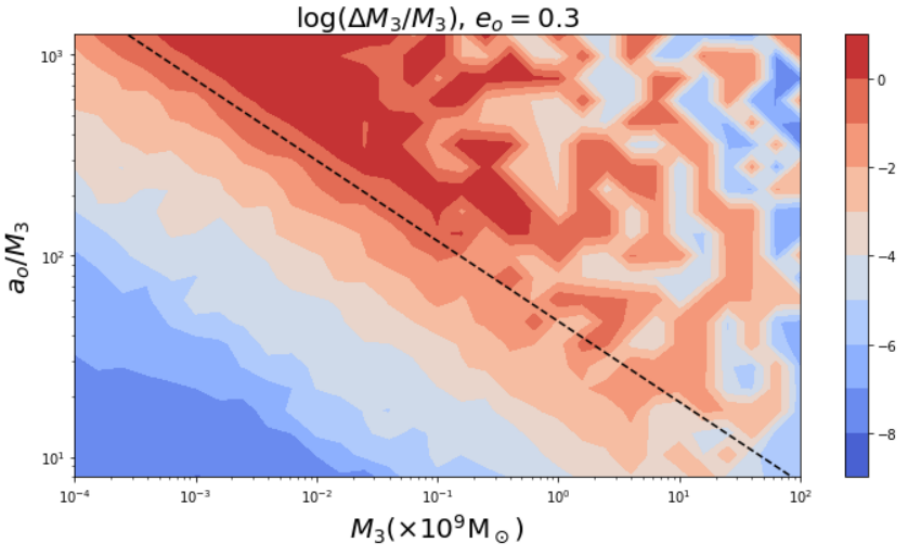

Figure 2: Fractional uncertainty in M_3 expected for a TianGO-like observatory with $e_o = 0.3$, and all other parameters equal to that in [4].

1.2 Development of Parameter Estimation Code

I have created a new version of the code used to compute the waveform of a BBH orbiting an SMBH with a circular outer orbit ($e_o = 0$) so that it now allows for eccentric outer orbits. This modification requires the addition of two parameters to the waveform (the eccentricity itself, and the argument of periapsis, which is undefined for a circular orbit). It also requires some basic analytic expressions for the precession of the BBH angular momentum $\vec{L}_i$ about the orbital angular momentum $\vec{L}_o$ to be modified into numerical integrations, as the precession frequency depends significantly on the distance of the BBH from the SMBH, and substitutes the ordinary expression for the position in a circular orbit as a function of time with Kepler's equation, which accounts for non-zero eccentricity (and thus a non-constant orbital angular frequency) and can be solved via iteration of Newton's method. I have confirmed that this new waveform code produces identical results to the older version when e_o is taken to be 0 and all other parameters are matched. With this confirmation complete, I am now looking to generate parameter estimation contour plots to obtain an understanding of how a non-circular outer orbit can change our ability to measure parameters of these hierarchical triples from the situation where $e_o = 0$.

2 Current results

Figure 2 shows the fractional uncertainty in the SMBH mass M_3 with an outer BBH orbit with eccentricity 0.3. All other parameters are identical to that used in Figure 5 of [4]. While I am continuing to look for the source of the patchy behavior seen above the $P_{dS} = 10$yr dashed line, the behavior of the plot below the line is promising. In comparison to Figure 5 of [4], there is a slight but broad improvement in the parameter estimation precision across the $(M_3, a_o/M_3)$ parameter space. This is consistent with our expectations: an eccentric outer orbit can produce more substantial waveform modulation due to both the wider range of possible Doppler phase shifts throughout the orbital path and the non-constant rate of de Sitter precession.

One detail that is worth noting is the set of parameters used to compute the waveform. The waveform can be reparametrized in terms of M_3 and $\Omega_o = \sqrt{GM_3/a_o^3}$ as opposed to M_3 and a_o. As it turns out, the orbital frequency Ω_o can be measured quite well (i.e., its diagonal element in the inverted Fisher matrix is very small) – much better than other parameters like M_3, for example – by TianGO as it orbits around the Sun, so in order to simplify the Fisher analysis, we can treat Ω_o (and other parameters with very small diagonal entries in $(\Gamma_{ij})^{-1}$) as perfectly well known. In practice, we therefore remove Ω_o from the parameters

in the Fisher matrix – this will allow us to reduce the magnitude range of values in the computed covariance matrix and thus potentially avoid numerical precision errors inherent to inverting matrices with such large magnitude ranges [3]. As it turns out, the two additional parameters introduced in an eccentric outer orbit – e_o and γ_o – along with T_o, can all be measured to high precision as well. So, when studying parameters which are not measured as well ($\log M_3$, for example), we can safely omit them from the Fisher matrix. This increases our computational efficiency in addition to the benefits described in [3].

3 Problems with numerical precision

In calculating the Fisher matrix, we compute the derivative of the waveform with respect to a wide set of parameters. These derivatives may vary by many orders of magnitude – in fact, in some of the Fisher matrices I have calculated, I have observed differences in scale approaching 10^{15} between certain terms. As such, the inversion of the Fisher matrix can be quite sensitive to slight errors, as the range in scale can magnify these errors substantially. In a high dimensional Fisher matrix (in our case, we frequently use 10 or more parameters), this concern is exacerbated, as described in [3]. As such, computing the Fisher matrix to high precision with numerical methods is a task of great importance.

It is well-known that the derivative of a function, by definition, is a limit, that is:

$$\partial_{\theta_i} h(\vec{\theta}) = \lim_{\Delta\theta_i \to 0} \frac{h(\vec{\theta} + \Delta\theta_i \hat{\theta}_i) - h(\vec{\theta} - \Delta\theta_i \hat{\theta}_i)}{2\Delta\theta_i} \tag{24}$$

where θ_i is a single parameter in the total set of parameters $\vec{\theta}$. In many scenarios, we can calculate this limit analytically, but when many parameters are involved, computing this result becomes overly complicated. Instead, we exploit the limit definition and choose some small value of $\Delta\theta_i \ll \theta_i$ and compute the expression above explicitly for that choice of $\Delta\theta_i$. However, this numerical method is not without its faults. If $\Delta\theta_i$ is taken to be too small, the change in h may be smaller than the numerical precision capable of the particular computer in use, and thus the derivative calculated may become orders of magnitude off its true value. On the other hand, if $\Delta\theta_i$ is too large, the approximation that h is roughly linear within a region of size $\Delta\theta_i$ of $\vec{\theta}$ (the fundamental assumption of the limit definition of the derivative) fails, and the calculated derivative will once again miss the true value. This suggests that there is a "sweet spot" for each parameter, where $\Delta\theta_i$ is small enough that h is roughly linear in $(\theta_i - \Delta\theta_i, \theta_i + \Delta\theta_i)$ but not too small that the change in h after the parameter adjustment falls below machine precision. In general, we expect that before the machine precision effects become prevalent, the error in the calculated derivative $\partial_{\theta_i} h|_{\text{true}} - \partial_{\theta_i} h[\Delta\theta_i]|_{\text{estimated}}$ should scale roughly as $\Delta\theta_i^2$.

Figure 3 is an example of how this appears in practice. Along the $x-$axis, various step sizes $\Delta \log d$ are used to estimate $\partial_{\log d} h$. The $y-$axis shows the fractional difference in computed derivative when a given $\Delta \log d$ is used compared to $4\Delta \log d$. From right to left, the point at which the quadratic form of the error gives way to the fluctuating form characteristic of machine precision errors, between $\Delta \log d = 2$ and 3×10^{-3}, is where we expect the most numerically-stable computation of $\partial_{\log d} h$. In other words, it is the smallest value of $\Delta \log d$ that can be used before numerical precision errors come into play, and thus, we choose a slightly larger value (say, 4×10^{-3} in our code).

However, this is only a simple case. In Figure 4, we display the same plot as above, except for computing $\partial_{\log \Omega_o} h$, where $\Omega_o = \sqrt{GM_3/a_o^3}$. For each evaluated frequency, there is some $\Delta \log \Omega_o$ at which the best numerical stability is attained, but these do not occur at the same step size. So, we cannot chose a step size for the computation of the derivative which yields an accurate result for all frequencies in our observing range. The Fisher matrix elements require integrating $\partial_{\theta_i} h$ over all frequencies in the observing range, so a single step size for a given parameter, evaluated at all frequencies, may prevent accurate computation of the inner products within the Fisher matrix. I am now working to determine whether a frequency-dependent step size for computation of the waveform derivative is necessary, or if some other statistic may show that a single $\Delta\theta_i$ for all frequencies is sufficient.

One potential option is the waveform mismatch, defined by

$$\mathcal{M}(h_1, h_2) = 1 - \mathcal{O}(h_1, h_2) \tag{25}$$

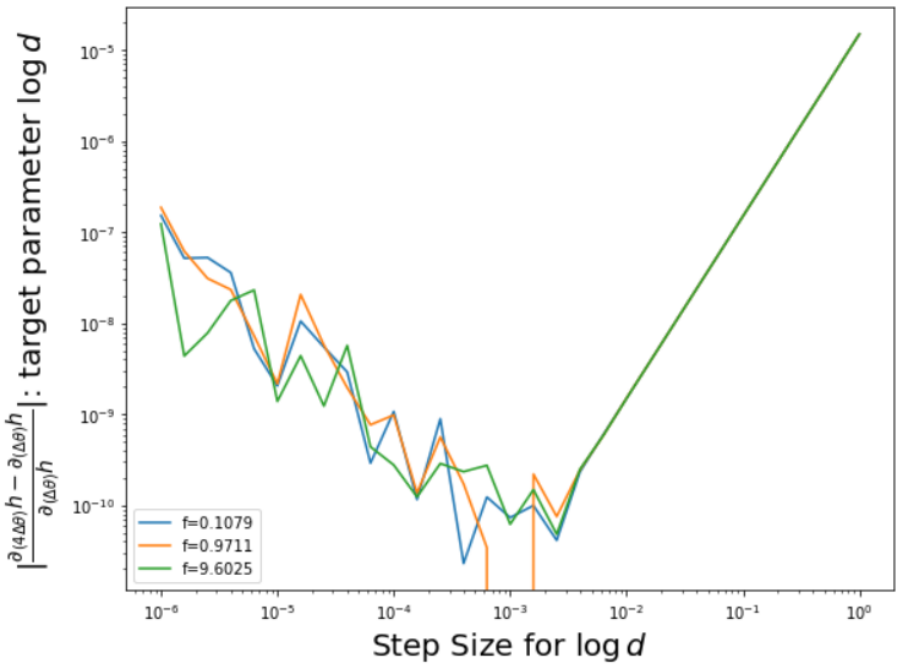

Figure 3: Fractional difference in computed derivative of h for a variety of step sizes $\Delta \log d$ and at three GW frequencies. The derivative of h when $\Delta \log d$ is used is compared to when $4\Delta \log d$ is used.

where

$$\mathcal{O}(h_1, h_2) \equiv \frac{(h_1 \mid h_2)}{\sqrt{(h_1 \mid h_1)(h_2 \mid h_2)}}, \tag{26}$$

The mismatch is 0 when the waveforms are aligned (specifically, when one is a constant multiple of the other). In our case, we examine the mismatch between the derivative of the waveform when two different step sizes are used to calculate ∂h. Usually, the step sizes are chosen to be $\Delta\theta_i$ and $k\Delta\theta_i$ where $k \sim$ a few. A small mismatch in this case indicates that at step size $\Delta\theta_i$, the derivative is quite stable to a change in the step size, and thus that the particular choice of $\Delta\theta_i$ is satisfactory (see Fig. 5). The mismatch is computed through integration over all frequencies, and is therefore a possible method to establishing a sufficient step size for each parameter in Fisher matrix computations.

4 Future directions

Given the complicated form of the strain measured by a TianGO-like space-based GW observatory, it is not surprising that the particular parameter estimation uncertainties, as calculated in the Fisher matrix approach, can depend heavily on angular parameters which may vary widely from system to system (i.e., $\overline{\theta}_S, \overline{\phi}_S, \overline{\theta}_J, \overline{\phi}_J, \lambda_L, \alpha_0, \gamma_o, T$). To make this study more general, I plan to average over some subset of these parameters so to mitigate the effects of the strong angular parameter dependencies. Each parameter averaged over multiplies the number of Fisher matrices which must be computed, so I will have to be judicious in choosing the most important candidate parameters so to avoid excessive computing times.

Finally, I will repeat the Fisher analysis to examine how our measurements of other parameters vary as the eccentricity of the outer orbit changes. At a basic level, I expect that the expanded range of Doppler phase shifts and faster de Sitter precession will lead to improved parameter estimation precession across all parameters, but again, the measured strain waveform is quite complicated, and this expectation may not hold uniformly.

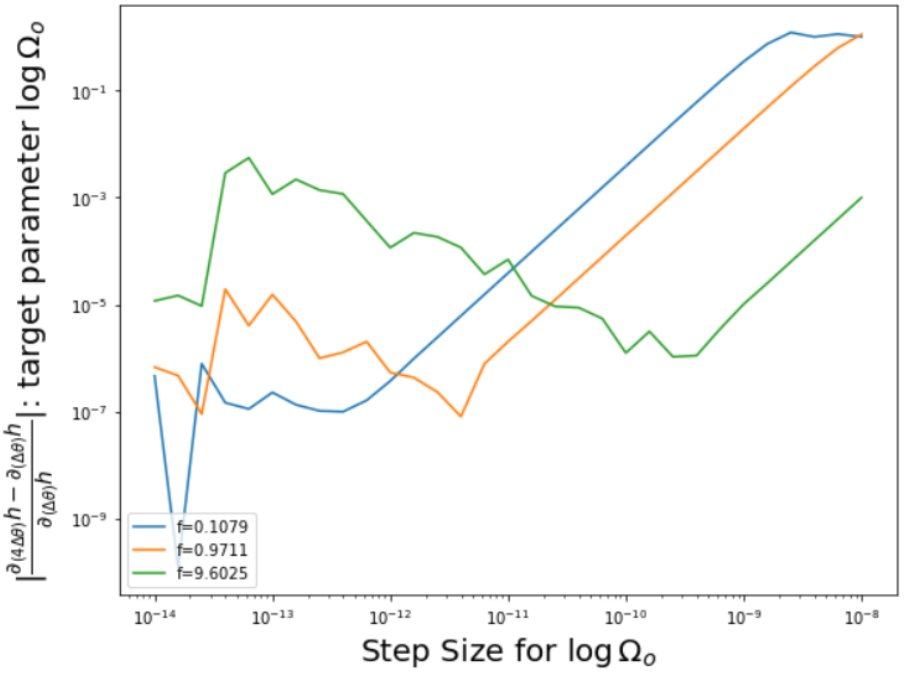

Figure 4: Fractional difference in computed derivative of h for a variety of step sizes $\Delta\log\Omega_o$ and at three GW frequencies. The derivative of h when $\Delta\log\Omega_o$ is used is compared to when $4\Delta\log\Omega_o$ is used.

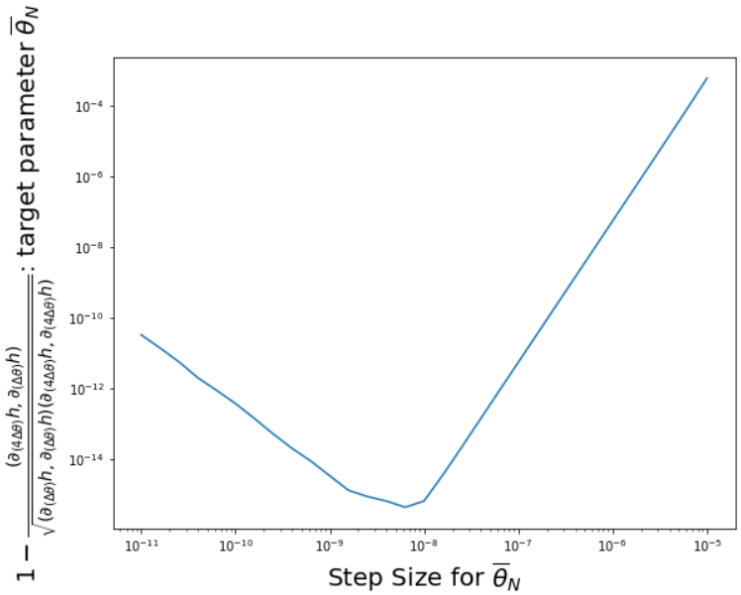

Figure 5: The mismatch between $\partial_{\overline{\theta}_S}h$ (written as θ_N here) when calculated with step size $\Delta\overline{\theta}_S$ and $4\Delta\overline{\theta}_S$. The turn in the plot near $\Delta\overline{\theta}_S \sim 10^{-8}$ suggests that this is a good choice for the step size in computing Fisher matrix terms involving $\overline{\theta}_S$.

5 Acknowledgments

I'd like to thank Brian Seymour and Yanbei Chen for their tremendous support in this project. I also gratefully acknowledge the support from the National Science Foundation Research Experience for Undergraduates (NSF REU) program, the California Institute of Technology, and the LIGO Summer Undergraduate Research Fellowship.

References

[1] Theocharis A. Apostolatos, Curt Cutler, Gerald J. Sussman, and Kip S. Thorne. Spin induced orbital precession and its modulation of the gravitational wave forms from merging binaries. *Phys. Rev. D*, 49:6274–6297, 1994.

[2] Eric Poisson and Clifford M. Will. *Gravity: Newtonian, Post-Newtonian, Relativistic*. Cambridge Univ. Press, 2014.

[3] Michele Vallisneri. Use and abuse of the Fisher information matrix in the assessment of gravitational-wave parameter-estimation prospects. *Phys. Rev. D*, 77:042001, 2008.

[4] Hang Yu and Yanbei Chen. Direct determination of supermassive black hole properties with gravitational-wave radiation from surrounding stellar-mass black hole binaries. *Phys. Rev. Lett.*, 126(2):021101, 2021.